AIAA Journal
Vol. 47, No. 5, May 2009

Direct Numerical Simulation of a Reflected-Shock-Wave/Turbulent-Boundary-Layer Interaction

S. Priebe,[*] M. Wu,[*] and M. P. Martín[†]
Princeton University, Princeton, New Jersey 08544

DOI: 10.2514/1.38821

A direct numerical simulation of a reflected-shock-wave/turbulent-boundary-layer interaction at Mach 2.9 and $Re_\theta = 2300$ with a flow deflection through the incident shock of 12 deg is presented. A modified weighted essentially nonoscillatory method is used for the spatial discretization of the inviscid fluxes. The numerical scheme has previously been validated in the direct numerical simulation of a compression-ramp interaction against experiments at matching conditions. The flowfield for the present simulation is visualized using a numerical schlieren technique, and a movie of the flow reveals the unsteady shock motion. From the wall-pressure signal in the interaction region and pressure measurements in the freestream, the characteristic low frequency of the shock motion is inferred and found to agree with a scaling previously proposed. The evolution of the mean and fluctuating flow quantities through the interaction is studied. It is observed that the turbulence levels are greatly amplified in the downstream flow and that significant departures from the strong Reynolds analogy occur.

Nomenclature

C_f = skin-friction coefficient
f = frequency
f_s = frequency of shock motion
J = Jacobian matrix of the grid transformation
L_{sep} = separation length
M = freestream Mach number
p = pressure
Re_δ = Reynolds number based on δ
Re_{δ^*} = Reynolds number based on δ^*
Re_θ = Reynolds number based on θ
S_{ij} = rate-of-strain tensor
S_L = dimensionless frequency of shock motion based on L_{sep} and U_∞
T = temperature
u = velocity in the streamwise direction
v = velocity in the spanwise direction
w = velocity in the wall-normal direction
x = coordinate in the streamwise direction
y = coordinate in the spanwise direction
z = coordinate in the wall-normal direction
δ = 99% thickness of the incoming boundary layer
δ^* = displacement thickness of the incoming boundary layer
θ = momentum thickness of the incoming boundary layer
ρ = density
$\langle\cdot\rangle$ = averaged quantity

Subscripts

rms = root-mean-squared quantity
w = value at the wall
∞ = freestream value

Superscript

$'$ = fluctuation from the mean
$*$ = nondimensional value
$+$ = nondimensionalization by inner (wake) scales

I. Introduction

THE interaction of a shock wave and a turbulent boundary layer (STBLI) is an important feature in many practically relevant compressible flows. Experiments of separated STBLI have shown (see Smits and Dussauge [1]) that the shock system exhibits a large-scale streamwise motion with a frequency that is 1 to 2 orders of magnitude less than the characteristic frequency of the turbulence in the incoming boundary layer. Recently, Wu and Martín [2,3] observed the low-frequency shock motion in a DNS of a 24 deg compression-ramp interaction at Mach 2.9 and $Re_\theta = 2300$. The practical importance of STBLI stems from the fact that at the wall along which the boundary layer is developing, the flow unsteadiness makes itself felt as large-amplitude low-frequency fluctuations of the pressure and heat transfer rate. In the case of super- and hypersonic flight, these fluctuations may well be detrimental to the structural and thermal integrity of the vehicle. The shock unsteadiness, together with other aspects of STBLI such as the turbulence amplification through the interaction, are not yet fully understood. A better understanding of STBLI is expected to lead to turbulence models that are true to the physics, flow control methodologies, and novel super- and hypersonic vehicle designs.

Most studies in the field of STBLI have been concerned with one of the canonical flow configurations such as the compression-ramp, reflected-shock, and fin interactions. In the present work, we consider the reflected-shock interaction in which an oblique shock, generated by some external source, impinges on a flat-plate turbulent boundary layer. This configuration is nominally two-dimensional. It is representative of, for example, the STBLI occurring in the air intakes of super- and hypersonic engines. Despite its practical importance, the reflected-shock interaction has received considerably less experimental attention than the compression-ramp configuration.

Green [4] performed experiments at Mach 2.5 and $Re_\delta = 4 \times 10^5$ for deflection angles through the incident shock varying from 2 to 10.5 deg. Measurements included surface-pressure distributions and pitot surveys, and the flow was visualized using surface oil, schlieren, and shadowgraph techniques. Two different interaction patterns were observed, depending on the strength of the incident

---

Received 29 May 2008; revision received 22 December 2008; accepted for publication 5 January 2009.

[*] Graduate Student, Department of Mechanical and Aerospace Engineering. Student Member AIAA.

[†] Assistant Professor, Department of Mechanical and Aerospace Engineering. Senior Member AIAA.

shock. For weak incident shocks (deflection angles up to 5 deg), the boundary layer remained attached and the shock reflected in an essentially inviscid fashion. For stronger incident shocks, however, the boundary layer separated and a more complicated interaction pattern resulted, involving the principal reflected shock followed downstream by an expansion fan and a sequence of compression waves near the point of flow reattachment.

The experiments by Green [4] are at a relatively high Reynolds number. Recently, a number of experiments have been performed at much lower Reynolds numbers, and these are of particular interest in the context of the present work, because they are within the reach of DNS. Dussauge et al. [5] investigated shock reflections at Mach 2.3 and $Re_\theta = 5900$ for deflection angles through the incident shock varying from 7 to 9.5 deg. Fluctuating wall-pressure measurements were made, and the low-frequency shock motion was analyzed. Particle image velocimetry (PIV) measurements in streamwise–spanwise planes revealed that the flow in the separation bubble is three-dimensional. Dupont et al. [6] carried out PIV for the same configuration in streamwise–wall-normal planes, and their results show the presence of large-scale vortical structures in the separated shear layer downstream of the reflected shock. These PIV data are not time-resolved, but using instantaneous visualizations, Dupont et al. found that the height of the separated-flow region and the shock position are correlated, with a larger height corresponding to an upstream location of the shock. This kind of statistical link between the extent of the separated-flow region and the shock motion has previously been observed in experiments and simulations of the compression-ramp configuration (see, for example, [3]).

Bookey et al. [7,8] and Ringuette et al. [9] performed experiments for a 12 deg incident shock impinging on a boundary layer at Mach 2.9 and $Re_\theta = 2400$. These flow conditions closely match the present DNS, allowing for a direct comparison between the two. Measurements in the experiments included surface-pressure distributions and pitot surveys; the flow was visualized using surface oil and CO_2-enhanced filtered Rayleigh scattering.

Garnier et al. [10] performed a large eddy simulation (LES) of a reflected STBLI at Mach 2.3 and $Re_{\delta^*} = 19{,}132$. The flow deflection through the incident shock was 8 deg. As noted by the authors, the simulation was not run for a long enough time to investigate the low-frequency shock motion. Touber and Sandham [11] also performed a LES of the reflected STBLI at Mach 2.3 and $Re_{\delta^*} = 2 \times 10^4$, matching the experimental conditions of Dussauge et al. [5]. The low-frequency shock unsteadiness is present in their simulations with a dimensionless frequency of around $S_L = 0.03$, and they studied various spanwise domain sizes to match the experimental separation length. Pirozzoli and Grasso [12] carried out a DNS of a reflected STBLI at Mach 2.25 and $Re_\theta = 3725$ for a deflection angle through the incident shock of 8.1 deg. A seventh-order-accurate weighted essentially nonoscillatory (WENO) scheme was used for the spatial discretization of the inviscid fluxes. At the inlet of the computational domain, a laminar profile was prescribed, and the flow was tripped to turbulence downstream by an alternating suction/blowing wall-boundary condition. Pirozzoli and Grasso proposed a mechanism whereby acoustic feedback in the separation bubble drives the shock motion. However, the low-frequency shock motion may not be captured in their DNS, because the lowest reported dimensionless shock frequency S_L is between 0.09 and 0.24. These values lie above the range of $S_L = 0.02$–0.05 found by Dussauge et al. [5] in a survey of STBLI experiments.

Wu and Martín [2] performed the DNS of a 24 deg compression-ramp flow at Mach 2.9 and $Re_\theta = 2300$. They validated their results (in terms of separation length, mean wall-pressure distribution, and evolution of the mean flow through the interaction) against experiments by Bookey et al. [7,8] at matching conditions. In addition, Ringuette et al. [13] validated the fluctuating wall pressure in the DNS against the experiments by Ringuette and Smits [14]. In the present work, we perform the DNS of a reflected STBLI. We use the same DNS code used by Wu and Martín [2] with the same incoming boundary-layer conditions and similar overall pressure rise.

The paper is organized as follows. In Sec. II, the governing equations are described, followed in Sec. III by a presentation of the computational setup. The DNS results are presented and discussed in Sec. IV, in which we describe the general features of the flowfield as well as analyze the turbulence amplification and shock motion. Finally, in Sec. V, conclusions are drawn.

II. Governing Equations

The governing equations are the nondimensionalized conservative form of the continuity, momentum, and energy equations in curvilinear coordinates. The working fluid is air, which is assumed to be a perfect gas.

$$\frac{\partial \boldsymbol{U}}{\partial t} + \frac{\partial \boldsymbol{F}}{\partial \xi} + \frac{\partial \boldsymbol{G}}{\partial \eta} + \frac{\partial \boldsymbol{H}}{\partial \zeta} = 0 \tag{1}$$

where

$$\boldsymbol{U} = J\left\{\begin{array}{c} \rho^* \\ \rho^* u^* \\ \rho^* v^* \\ \rho^* w^* \\ \rho^* e^* \end{array}\right\}, \qquad \boldsymbol{F} = \boldsymbol{F}_c + \boldsymbol{F}_v \tag{2}$$

and

$$\boldsymbol{F}_c = J r_\xi \left\{\begin{array}{c} \rho^* u^{*'} \\ \rho^* u^* u^{*'} + p^* s_x^* \\ \rho^* v^* u^{*'} + p^* s_y^* \\ \rho^* w^* u^{*'} + p^* s_z^* \\ (\rho^* e^* + p^*) u^{*'} \end{array}\right\}$$

$$\boldsymbol{F}_v = -J r_\xi \left\{\begin{array}{c} 0 \\ \sigma_{xx}^* s_x^* + \sigma_{xy}^* s_y^* + \sigma_{xz}^* s_z^* \\ \sigma_{yx}^* s_x^* + \sigma_{yy}^* s_y^* + \sigma_{yz}^* s_z^* \\ \sigma_{zx}^* s_x^* + \sigma_{zy}^* s_y^* + \sigma_{zz}^* s_z^* \\ (\sigma_{xx}^* u^* + \sigma_{xy}^* v^* + \sigma_{xz}^* w^*) s_x^* \\ +(\sigma_{yx}^* u^* + \sigma_{yy}^* v^* + \sigma_{yz}^* w^*) s_y^* \\ +(\sigma_{zx}^* u^* + \sigma_{zy}^* v^* + \sigma_{zz}^* w^*) s_z^* \\ -q_x^* s_x^* - q_y^* s_y^* - q_z^* s_z^* \end{array}\right\} \tag{3}$$

and

$$s_x^* = \xi_x / r_\xi, \qquad u^{*'} = u^* s_x^* + v^* s_y^* + w^* s_z^*$$
$$r_\xi = \sqrt{\xi_x^2 + \xi_y^2 + \xi_z^2} \tag{4}$$

In curvilinear coordinates, the flux terms G and H have similar forms to F. The stress tensor σ_{ij}^* is given by the Newtonian linear stress–strain relation:

$$\sigma_{ij}^* = \frac{1}{Re_\delta}\left(2\mu^* S_{ij}^* - \frac{2}{3}\mu^* \delta_{ij} S_{kk}^*\right) \tag{5}$$

The heat flux terms q_j^* are given by the Fourier law:

$$q_j^* = -\frac{1}{Re_\delta} k^* \frac{\partial T^*}{\partial x_j^*} \tag{6}$$

The dynamic viscosity is computed by Sutherland's law:

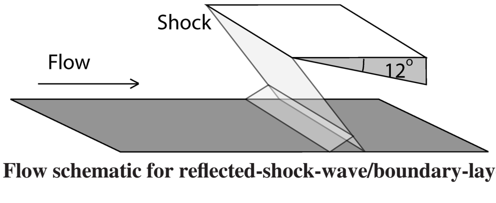

Fig. 1 Flow schematic for reflected-shock-wave/boundary-layer interaction.

Table 1 Conditions for the incoming turbulent boundary layer

	M	Re_θ	θ, mm	δ^*, mm	C_f	δ, mm	ρ_∞, kg/m^3	U_∞, m/s	T_∞, K
Experiment [7,8]	2.9	2400	0.43	2.36	0.00225	6.7	0.074	604.5	108.1
DNS	2.9	2300	0.38	1.80	0.00217	6.4	0.077	609.1	107.1

$$\mu = 1.458 \times 10^{-6} T^{3/2}/(T + 110.3) \tag{7}$$

The nondimensionalization is done by $\rho^* = \rho/\rho_\infty$, $u^* = u/U_\infty$, $e^* = e/U_\infty^2$, $p^* = p/\rho_\infty U_\infty^2$, $T^* = T/T_\infty$, and $\mu^* = \mu/\mu_\infty$. The thickness of the incoming boundary layer, δ, is used as the characteristic length scale.

III. Computational Setup

A schematic of the flow configuration for the present DNS is shown in Fig. 1. Note that the wedge-shaped shock generator is depicted for conceptual clearness only and is not included in the DNS. Instead, the incident shock is generated by imposing the appropriate Rankine–Hugoniot jump conditions at the inlet of the computational domain. The flow deflection through the incident shock is 12 deg in the DNS. The incoming boundary layer is at Mach 2.9 and $Re_\theta = 2300$, which closely matches experiments [7,8] for the same configuration (see Table 1).

Figure 2 shows the computational domain, which measures 20δ in the streamwise direction, 2δ in the spanwise direction, 9.5δ in the wall-normal direction at the inlet, and 9.9δ at the outlet. To minimize errors in the computation of the Jacobian matrices, the grid is computed from analytical transformations, details of which are given by Wu and Martín [2]. A sample grid is shown in Fig. 3. In the DNS, the number of grid points is $1100 \times 160 \times 132$ in the streamwise, spanwise, and wall-normal directions, respectively, but for clarity of presentation, the sample grid in Fig. 3 only shows every 32nd grid point in the streamwise direction and every 8th in the wall-normal direction. The grid is clustered near the wall in the wall-normal direction and near the interaction region in the streamwise direction, in which the range of the interaction region has been estimated from the experiments [7,8]. The largest and smallest grid spacings in the streamwise direction are $\Delta x^+ = 9.0$ and 4.3, respectively, with grid points clustered near $x = 9\delta$. At the inlet of the computational domain, the first grid point above the wall is at $z^+ = 0.2$. The grid is uniform in the spanwise direction with $\Delta y^+ = 3.9$.

Because the numerical method in the present DNS is identical to that used by Wu and Martín [2] for the DNS of a 24 deg compression ramp, we give only a brief description here. For the spatial discretization of the inviscid fluxes, a fourth-order-accurate WENO scheme is employed. The scheme is bandwidth-optimized (see Martín et al. [15]). In addition, it uses limiters to reduce the nonlinear error resulting from overadaptation of WENO in smooth regions of the flow (see Taylor et al. [16]). Wu and Martín [2] reported that the original WENO (without limiters) is too dissipative for accurate DNS of STBLI. For their compression-ramp DNS, they found that a combination of absolute and relative limiters is necessary to sufficiently reduce the dissipation of the numerical scheme. The same limiters are used here. For the spatial discretization of the viscous fluxes, a fourth-order-accurate central-difference scheme is used. Time integration is performed with a third-order-accurate low-storage Runge–Kutta algorithm.

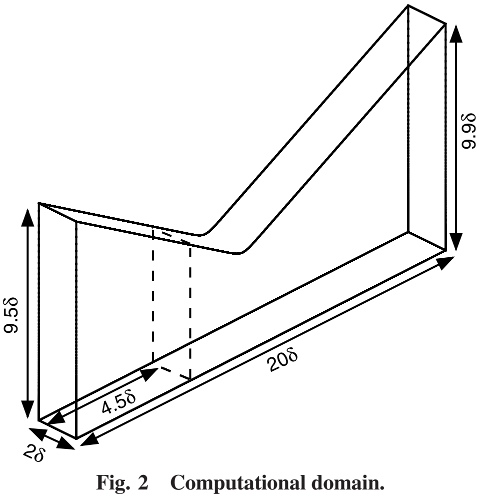

Fig. 2 Computational domain.

Except for the incident shock, which is imposed as a boundary condition at the inlet to the computational domain, the boundary conditions are identical to those used by Wu and Martín [2] for the compression-corner case. At the wall, a no-slip condition is used and a temperature of $T_{\text{wall}} = 307$ K is prescribed. At the inlet, the rescaling technique of Xu and Martín [17] is used. The recycling station is located 4.5δ downstream from the inlet, as indicated in Fig. 2. At the outlet and on the top boundary, a supersonic exit condition is used; periodic boundary conditions are employed in the spanwise direction. The boundary layer is initialized using the method of Martín [18]. In this method, a set of coherent vortical turbulence structures is introduced in the domain. By the law of Biot–Savart, these structures induce an initial pressure field. We have found that this results in a small level of uncorrelated noise that gets carried through the simulation, unless it is filtered. This has been discussed in the context of the compression corner (Ringuette et al. [13]), in which the same initialization is used and the level of uncorrelated noise is found to be 4% in the magnitude of wall-pressure fluctuations. Experiments show a noise level of 2% for the same flow (see Ringuette and Smits [14]). The same level of uncorrelated noise (4%) is found in the present simulations.

IV. DNS Results

Statistics are gathered using 561 flowfields spanning a total time of $975\delta/U_\infty$ (i.e., approximately 10 ms). Figure 4 shows a typical instantaneous numerical schlieren (NS) plot, in which the variable is defined as

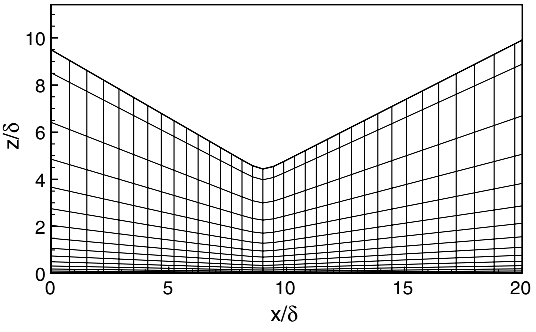

Fig. 3 Sample grid.

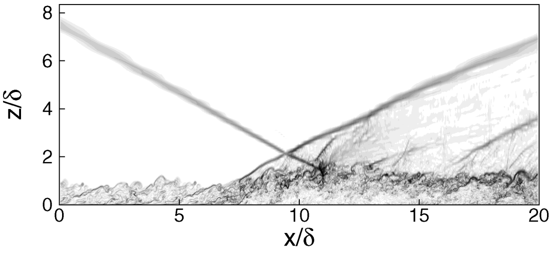

Fig. 4 Instantaneous numerical schlieren for the DNS.

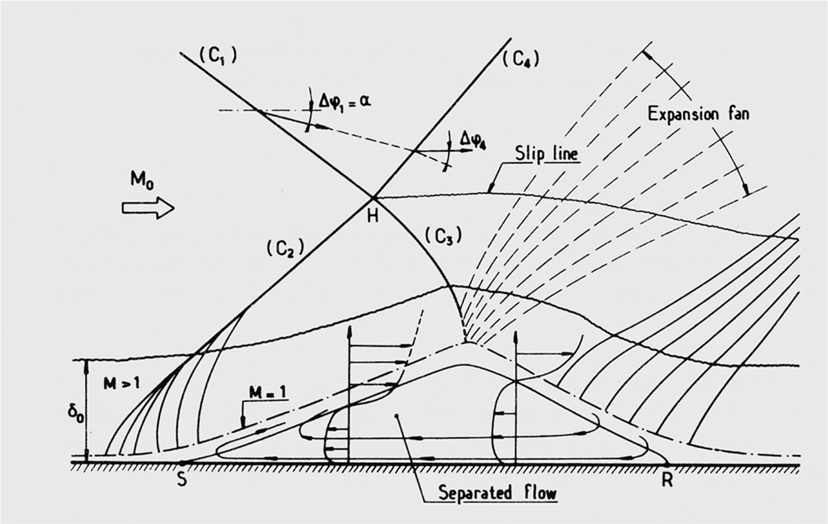

Fig. 5 Flow schematic for the reflected-shock-wave/boundary-layer interaction with separation (from Délery and Marvin [19]).

$$\mathrm{NS} = c_1 \exp[-c_2(x - x_{\min})/(x_{\max} - x_{\min})] \tag{8}$$

where $x = |\nabla \rho|$ and c_1 and c_2 are constants. We use $c_1 = 0.8$ and $c_2 = 10$ in our analysis. This transformation enhances small density gradients in the flowfield and resembles experimental schlieren visualizations. A notable feature of the interaction is that the reflected shock originates well upstream of the point at which the incident shock impacts the boundary layer. This upstream influence may be understood from the flow sketch in Fig. 5, which illustrates the principal features of a reflected-shock-wave/boundary-layer interaction in the case in which separation is present (taken from Délery and Marvin [19]). The pressure gradient imposed by the shock is felt upstream through the subsonic portion of the flow, causing the boundary layer to separate well upstream of the shock impact point. Given the presence of the separation bubble, the boundary layer is constrained to move away from the wall, and the turning of the flow leads to a series of compression waves emanating from the region near the separation point (denoted by S in the flow sketch). Further away from the wall, these waves coalesce to form the principal reflected shock. In addition to the principal reflected shock, the flow sketch in Fig. 5 shows two further left-running wave groups: namely, an expansion fan and a sequence of compression waves in the downstream flow. The expansion fan originates at the point at which the incident shock impacts the sonic line, which is also where the separation bubble obtains its maximum height (typically of order δ). Through the expansion fan, the flow is turned back into the wall, causing it to reattach downstream. Near the reattachment point (denoted by R in the sketch), a sequence of compression waves realigns the flow with the wall.

Although the expansion fan is not discernible in the instantaneous numerical schlieren plot in Fig. 4, a sequence of compression waves can clearly be seen in the downstream flow. Some of these compression waves are seen to merge into the reflected shock, whereas others originating closer to the exit of the computational domain do not merge into the reflected shock within the extent of the computational domain. The reflected shock is inclined at an angle of only 33 deg at the exit of the computational domain, which is below the inviscid value of 36 deg, as the computational domain is not long enough for the shock to reach the inviscid strength.

A movie of subsequent schlieren visualizations[‡] shows that the shock foot undulates at a high frequency. The undulations are seen to travel in the tangential direction along the shock, and with increasing distance from the wall, they are increasingly damped. Sufficiently far away from the wall, in the freestream, little undulations persist and the shock exhibits a low-frequency large-scale motion in the streamwise direction.

The shock motion is also apparent from Fig. 6, which shows a time- and spanwise-averaged numerical schlieren plot for the entire DNS data set. The reflected shock appears smeared, particularly near the foot, owing to the unsteadiness. It is apparent from both the instantaneous and the mean schlieren visualizations that downstream of the interaction, the density gradients are steeper, illustrating the turbulence amplification through the shock system.

Figure 7 shows a typical instantaneous isosurface of the magnitude of pressure gradient $|\nabla p| = 0.25 p_\infty/\delta$ for the DNS. It illustrates the three-dimensional structure of the interaction. Away from the wall, in the freestream, the reflected-shock sheet is quite uniform in the spanwise direction. This must be contrasted with the shock foot, which exhibits significant spanwise-wrinkling. In the particular instantaneous realization shown in Fig. 7, a bulge is visible in the foot region of the reflected-shock sheet (the bulge is highlighted by a circle in Fig. 7).

The time- and spanwise-averaged skin-friction coefficient C_f is plotted against streamwise distance in Fig. 8a. Results are shown for the present reflected-shock DNS as well as for the 24 deg compression-ramp DNS of Wu and Martín [2], centering both profiles at the mean-flow separation point. Using the zero-skin-friction criterion, we find that the mean-flow separation point for the present DNS is located at $x = 7.0\delta$, where x is measured from the inlet of the computational domain; the mean-flow reattachment point is located at $x = 14.6\delta$, giving a separation length of $L_{\mathrm{sep}} = 7.6\delta$. This may be compared with the compression-ramp DNS [2], where $L_{\mathrm{sep}} = 4.2\delta$. The separation length in the compression-ramp DNS is thus shorter, by a factor of 1.8, than in the present reflected-shock DNS. Such a direct comparison between the two configurations is meaningful, because the incoming flow conditions are identical (Mach 2.9 and $Re_\theta = 2300$) and the overall strength of the interactions is similar. Green [20] showed that a reflected-shock interaction with initial flow deflection α and a compression ramp of angle 2α have similar overall strength (i.e., the inviscid pressure recovered downstream is similar). In addition to the difference in

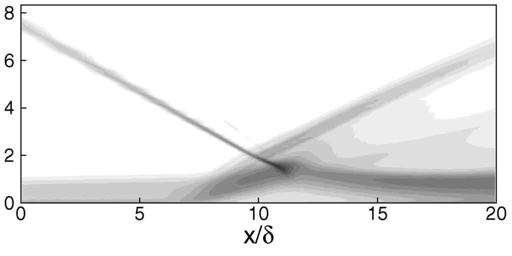

Fig. 6 Time- and spanwise-averaged numerical schlieren for the DNS.

[‡] Available online at http://www.princeton.edu/mae/people/faculty/martin/homepage/data-sets/movies/ [retrieved 30 September 2008].

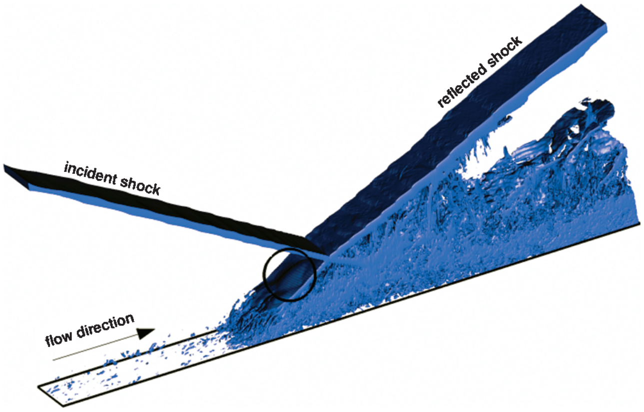

Fig. 7 Isosurface of the magnitude of pressure gradient $|\nabla p| = 0.25p_\infty/\delta$ showing the three-dimensional structure of the interaction for the DNS. The circle highlights a bulge in the reflected-shock sheet.

separation length, the skin-friction increases more rapidly downstream of reattachment in the compression-ramp case than in the reflected-shock case.

Figure 8b compares the mean wall-pressure distribution for the present reflected-shock DNS and the compression-ramp DNS of Wu and Martín [2]. The pressure profiles have been shifted in the streamwise direction to make the initial pressure rises coincide. The origin of the coordinate system used in Fig. 8b corresponds to the location of the domain inlet in the reflected-shock DNS, and $x = 9.8\delta$ is the location of the corner in the compression-ramp DNS. It is apparent that the initial pressure rise is nearly identical in both simulations. Furthermore, the pressure profiles exhibit a plateau in both cases, which is indicative of separated flow. Although the plateau pressure levels are similar, the streamwise extent of the plateau is greater for the reflected-shock DNS than for the compression-ramp DNS. This is consistent with the difference in separation length between the two simulations, which was observed previously from the C_f distribution (Fig. 8a). Downstream of the separation region, the pressure increases gradually toward the inviscid postshock pressure. The computational domain is not long enough to see the complete recovery.

From a survey of experimental results for different STBLI configurations covering a range of Mach and Reynolds numbers, Dussauge et al. [5] found that the frequency of the shock motion scales with the length of the separation bubble, L_{sep}, and the freestream velocity U_∞; that is,

$$S_L = \frac{f_s L_{\mathrm{sep}}}{U_\infty} \tag{9}$$

where the range of values found in the survey is $S_L = 0.02$–0.05.

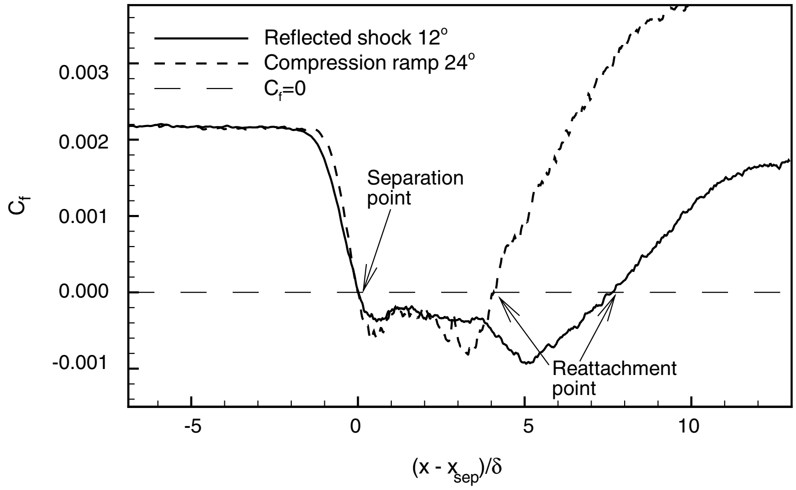

a)

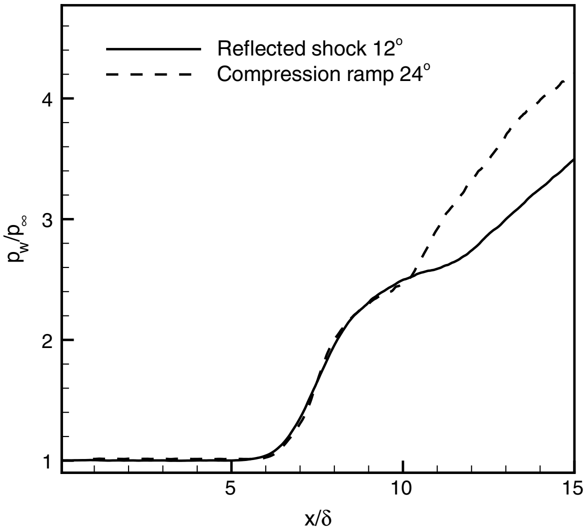

b)

Fig. 8 Plots of a) time- and spanwise-averaged C_f distribution and b) mean wall-pressure distribution. For comparison, the DNS results of Wu and Martín [2] are also shown for a 24 deg compression ramp at Mach 2.9 and $Re_\theta = 2300$.

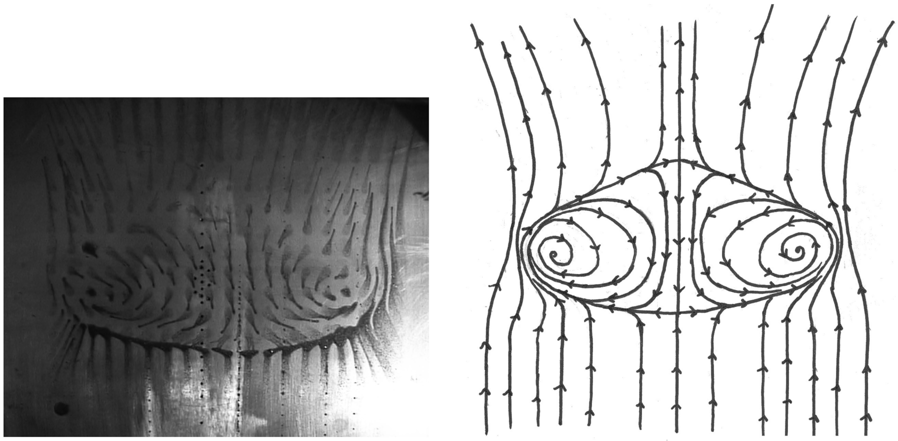

Fig. 9 Three-dimensional flow pattern observed in experiments [8]: a) surface flow visualization and b) sketch of the surface streamline pattern.

From wall-pressure spectra and mass-flux measurements in the freestream, Wu and Martín [2,3] found that in their DNS of a 24 deg compression ramp the shock exhibited a low-frequency motion in the range of $0.007–0.013U_\infty/\delta$. This corresponds to a Strouhal number of $S_L = 0.03–0.05$, which is in agreement with the range of values found by Dussauge et al. [5]. Because the separation length in the present reflected-shock DNS is larger by a factor of 1.8 than in the compression-ramp DNS, it is expected that, in accordance with the scaling in Eq. (9), the frequency of the shock motion will be lower by the same factor. We thus expect to have a low-frequency shock motion in the range of $0.004–0.007U_\infty/\delta$ in the present DNS. This is verified and discussed in more detail subsequently when we analyze the shock motion. Note that the DNS of the reflected-shock case is computationally more expensive than that of the compression-ramp case for two reasons: First, the reflected-shock interaction has a larger extent in the streamwise direction (as indicated by the larger separation length), thus requiring a spatially larger computational domain. Second, the preceding scaling argument indicates, and the subsequent DNS results confirm, that the shock frequency is lower, thus requiring the DNS to be run for a longer time to capture the shock motion.

Figure 9 shows surface flow visualizations from experiments [7,8] for a 12 deg reflected-shock configuration at conditions matching those of the present DNS (see Table 1). The separation length is seen to vary significantly in the spanwise direction, indicating that the flow is three-dimensional. There are two principal reasons for this: the shock generator used in the experiments does not span the entire width of the wind tunnel, and the flow is affected by the boundary layers developing on the tunnel sidewalls. Significant flow three-dimensionality is also seen in the experiments by Dussauge et al. [5] for a 9.5 deg shock impinging on a turbulent boundary layer at $M = 2.3$ and $Re_\theta = 5900$. In addition to observing a surface flow pattern similar to that shown in Fig. 9, PIV measurements reveal a highly-three-dimensional downstream flow with a pair of tornado-like vortices extending to a height of approximately 0.5δ above the wall.

Although the present DNS and the experiments [7,8] are nominally at the same conditions, it is clear that the actual flows are fundamentally different. The experimental flow is seen to be three-dimensional, whereas the numerical flow is homogeneous in the spanwise direction, in which periodic boundary conditions are used. As a result, no direct comparison is possible. Performing a DNS including the experimental spanwise length and wind-tunnel side-wall boundary conditions is not feasible. To illustrate the differences between the DNS and experiments further, the mean wall-pressure distributions are plotted in Fig. 10. The experimental data [7,8] have been obtained along the centerline of the interaction in which the streamwise extent of the separation bubble is largest, as can be seen form the surface oil visualizations in Fig. 9. No reference point is given in the experiments. Therefore, the profile from the experiments is shifted in the streamwise direction to make the two profiles match at separation. It is apparent from Fig. 10 that the pressure plateau is significantly longer in the experiments than in the DNS. This is consistent with the fact that in the experiments, the separation length is found to be 10.5δ along the tunnel centerline, which is significantly larger than the value of 7.6δ observed in the DNS.

Although direct validation of the DNS against the experiments [7,8] is not possible, we stress that because the simulation code is general and shock-location-independent and has been validated by Wu and Martín [2] for the compression-corner case, we perform the present DNS of the reflected-shock case with confidence.

The shock motion may be inferred from wall-pressure signals. Figure 11a shows the wall-pressure signals at different streamwise locations for the DNS. Of particular interest is the signal at the location $x = 7.1\delta$, which is near the mean-flow separation point. At this location, the pressure is seen to oscillate with a low frequency between the upstream value (as represented in the plot by the signal at the location $x = 2\delta$) and the value downstream of the reflected shock (as represented in the plot by the signal at the location $x = 9.5\delta$). This large-amplitude low-frequency oscillation of the wall pressure at $x = 7.1\delta$ may be attributed to the motion of the shock across this point. We draw attention to the fact that the present DNS is at low Reynolds number and the pressure trace at $x = 7.1\delta$ varies relatively smoothly between the upstream and downstream states. It does not show the intermittency that is typical in high-Reynolds-number flows (see also Wu and Martín [2] and Ringuette et al. [13]).

The premultiplied power spectra for the pressure signals are shown in Fig. 11b. The spectra are normalized by the square of the local mean wall pressure, and they have been bin-smoothed using

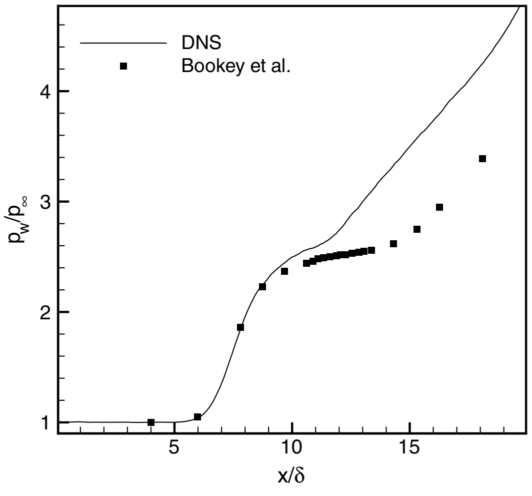

Fig. 10 Mean wall-pressure distribution from DNS and experimental data (Bookey et al. [7,8]).

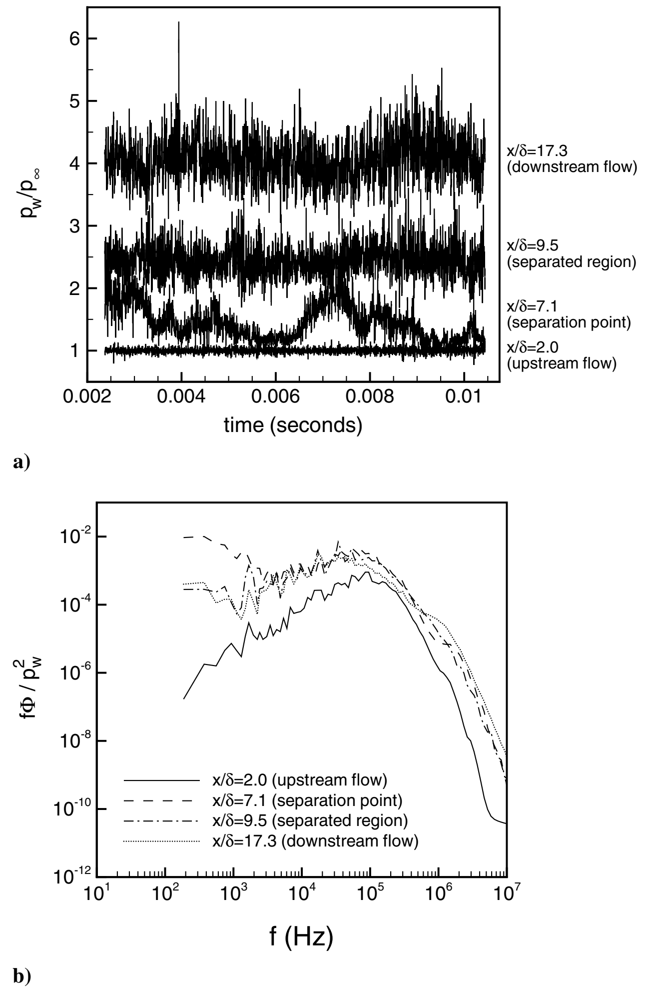

Fig. 11 Plots of a) wall-pressure signals at different streamwise locations and b) corresponding spectra for the DNS.

100 bins. In the incoming boundary layer, at $x = 2\delta$, the most energetic frequency is broadband in the range of 0.1–$1U_\infty/\delta$ (10–100 kHz) and is due to the turbulence. The spectrum for the location $x = 7.1\delta$, near the mean-flow separation point, also has significant energy in this range, but the dominant frequency is much lower. It lies in the range of 0.002–$0.006U_\infty/\delta$ (190–560 Hz) and may be attributed to the low-frequency shock motion. Further downstream, in the separated flow ($x = 9.5\delta$) and past the reattachment point ($x = 17.3\delta$), the spectra show less energy content at the low frequency of the shock motion, although it is still significant as compared with the upstream boundary layer. However, the most dominant frequency has shifted back to the range associated with the turbulent motions.

The frequency of the shock motion has thus been inferred from the wall-pressure signals to be 0.002–$0.006U_\infty/\delta$. This corresponds to a Strouhal number of $S_L = 0.015$–0.046, which is in the range of values given by Dussauge et al. [5].

A. Boundary-Layer Evolution

Figure 12 plots van Driest-transformed mean velocity profiles at different streamwise locations. In the incoming boundary layer, the velocity profiles show a logarithmic region that extends from approximately $z^+ = 30$ to 90. The relatively small extent of the logarithmic region is attributable to the low Reynolds number in the DNS. Because wall-scaling has no physical justification in separated flow, no profiles are given in the region $x = 7.0$–14.6δ, where the mean flow is separated. Three profiles are shown in the flow downstream of mean-flow reattachment ($x = 15.4\delta$, 16.9δ, and 17.7δ), all of which display a characteristic dip below the log law, indicating that the boundary layer is out of equilibrium and does not recover within the length of the computational domain. The characteristic dip below the log law has also been observed in the DNS of a compression ramp by Wu and Martín [2], as well as in compression-ramp experiments at high Reynolds numbers (see, for example, Smits and Muck [21]).

Figure 13 plots the mass-flux turbulence intensity at different streamwise locations for the DNS. Downstream of the interaction, the mass-flux turbulence intensity is amplified by a maximum factor of about 4. This may be compared with an amplification factor of 5 reported by Wu and Martín [2] for the DNS of the compression-ramp case with identical inflow condition and similar overall pressure rise through the interaction. A notable difference between the two configurations, however, is that the compression-ramp configuration involves streamline curvature, whereas in the reflected-shock configuration, there is no net streamline curvature. According to Smits and Dussauge [1], concave streamline curvature is expected to enhance turbulence amplification, and this may well explain why the maximum mass-flux turbulence amplification factor is found to be larger in the compression-ramp DNS than in the present reflected-shock DNS. Also from Fig. 13, in the separated-flow region ($x = 10\delta$), the peak of the mass-flux turbulence intensity occurs at $z = 1.2\delta$ above the wall. This location agrees well with the location of the mean-flow sonic line, which lies just above the edge of the separation bubble. Consequently, it may be hypothesized that the peak in the mass-flux turbulence intensity is due to turbulent structures in the separated shear layer. Further downstream, the peak in the mass-flux turbulence intensity is seen to move closer to the wall.

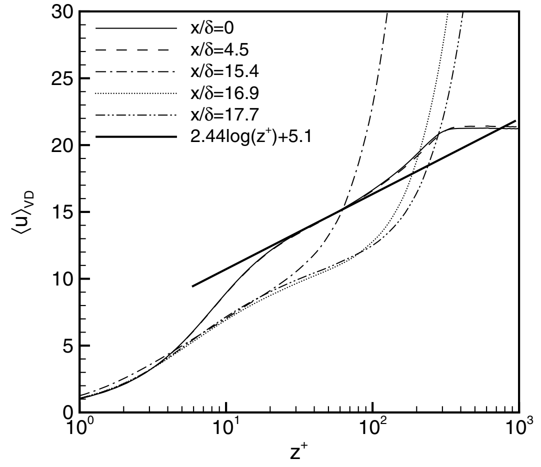

Fig. 12 Van Driest-transformed mean velocity profiles at different streamwise locations for the DNS.

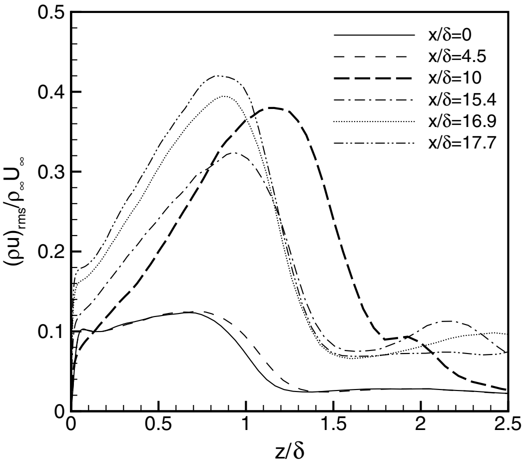

Fig. 13 Mass-flux turbulence intensities at different streamwise locations for the DNS.

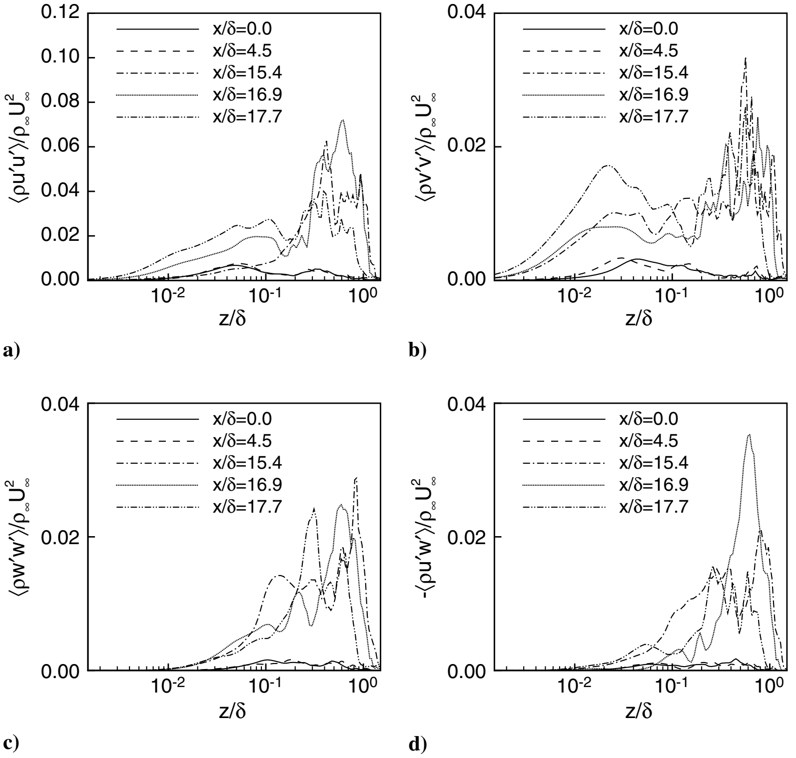

a)

b)

c)

d)

Fig. 14 Reynolds stresses at different streamwise locations for the DNS.

Figure 14 plots various components of the Reynolds stress tensor at different streamwise locations for the DNS. It is apparent that the Reynolds stresses are amplified significantly through the interaction. In particular, the streamwise component $\rho u'u'$ and the spanwise component $\rho v'v'$ are amplified by a maximum factor of about 10. The wall-normal component $\rho w'w'$ is amplified slightly more, by a maximum factor of about 18. The largest amplification factor is seen in the shear component $\rho u'w'$ and is about 21. These values may once again be compared with the DNS of the compression ramp by Wu and Martín [2]. It is important to note, however, that the reference values for the Reynolds stresses in the incoming boundary layer that were observed by Wu and Martín are different from those observed in the present reflected-shock DNS, although the incoming boundary-layer conditions are the same. This may be explained by the fact that Wu and Martín used less samples and that their stress profiles were less converged than those reported here. To allow for direct comparison between the two data sets, we have recomputed the amplification factors reported by Wu and Martín using the upstream reference values for the Reynolds stresses observed in the present DNS. We find that the observed maximum amplification factors for $\rho u'u'$, $\rho w'w'$, and $\rho u'w'$ are smaller in the present reflected-shock DNS than in the compression-ramp DNS (i.e., the amplification factor is about 10 for $\rho u'u'$ in the present DNS, as compared with 12 in the compression-corner DNS, 18 vs 22 for $\rho w'w'$, and 21 vs 27 for $\rho u'w'$). For $\rho v'v'$, the observed amplification factor is slightly larger in the reflected-shock DNS (10, as compared with 8 for the compression-ramp DNS).

The strong Reynolds analogy (SRA) relates the velocity fluctuations in a turbulent boundary layer to the temperature fluctuations. The SRA relations are given by

$$\frac{\sqrt{\langle T'^2\rangle}}{\tilde{T}} = (\gamma - 1)M^2 \frac{\sqrt{\langle u'^2\rangle}}{\tilde{u}} \tag{10}$$

$$R_{uT} = \frac{\langle u'T'\rangle}{\sqrt{\langle u'^2\rangle}\sqrt{\langle T'^2\rangle}} = \text{constant} \tag{11}$$

where a tilde in the equations denotes Favre-averaging. Figure 15 shows

$$\frac{T'_{\mathrm{rms}}\tilde{u}}{(\gamma - 1)M^2 u'_{\mathrm{rms}}\tilde{T}}$$

and R_{uT} at different streamwise locations for the DNS. It is apparent from Fig. 15a that in the incoming flow, the SRA relations are satisfied over most of the boundary layer, with R_{uT} approximately equal to -0.7. A significant departure from the SRA only occurs near the wall and close to the boundary-layer edge. Inside the interaction region, at $x = 8.5\delta$ and 13.8δ, the SRA relations are still satisfied reasonably well in the outer part of the boundary layer ($z > 0.5\delta$), whereas they do not hold in the inner part. Figure 15d plots the SRA relations at $x = 16.9\delta$, downstream of the mean-flow reattachment point. It is apparent that although the flow shows signs of recovering to the equilibrium behavior seen upstream, major departures from the SRA are still present, particularly in the inner part of the boundary layer ($z < 0.5\delta$). This corroborates the conclusion, drawn previously by looking at the van Driest-transformed velocity profiles, that the flow downstream of the interaction does not recover to equilibrium within the length of the computational domain.

Figure 16a plots $-R_{uT}$ at different wall-normal locations for the present DNS. The data at $z^+ = 20$ are qualitatively different from the other wall-normal locations in that these data do not display a leading peak near the point of mean-flow separation. These kinds of qualitative differences are not unexpected, because the location $z^+ = 20$ lies in the near-wall region, in which significant departures from the SRA relations have been observed in the discussion of Fig. 15. For all other wall-normal locations, a peak in the value of $-R_{uT}$ is observed near the mean-flow separation point. The magnitude of this peak increases with increasing distance from the wall and its location shifts slightly downstream. Presumably, it is the presence of the reflected-shock foot that causes this peak. Another notable feature of the distributions of $-R_{uT}$ is a minimum located in the separated-flow region, which presumably is due to the presence of the incident shock. It is apparent that the magnitude of the minimum decreases with increasing distance from the wall. Downstream of the mean-flow reattachment point, there are signs of a recovery toward the upstream equilibrium. For the outermost locations shown ($z = 0.5\delta$, 0.7δ, and 0.9δ), values close to the upstream equilibrium value are attained at the exit of the computational

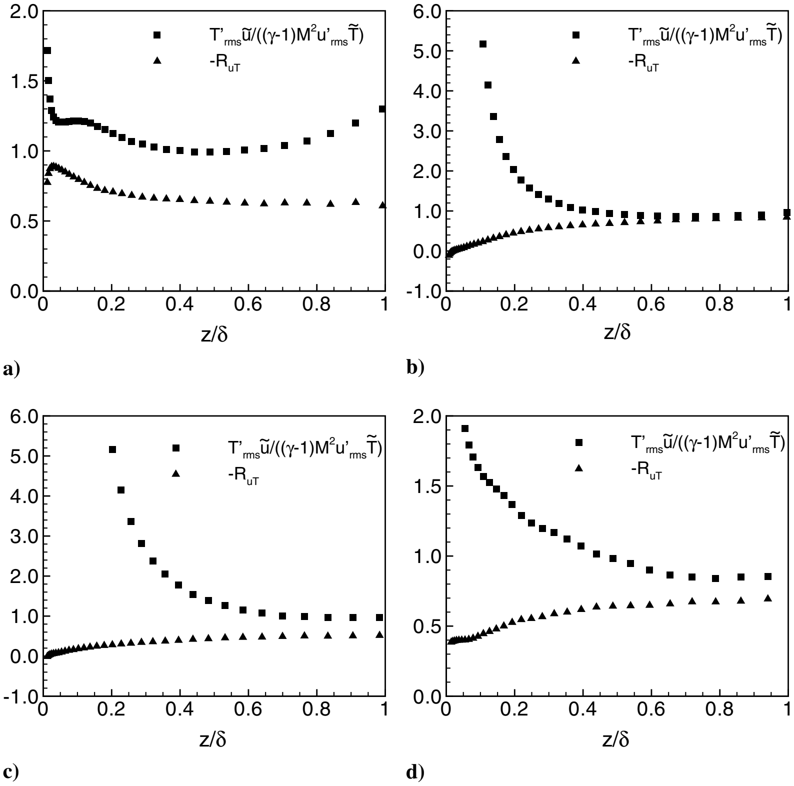

a) b) c) d)

Fig. 15 SRA [Eqs. (10) and (11)] at different streamwise locations for the DNS: a) $x = 4.6\delta$, b) $x = 8.5\delta$, c) $x = 13.8\delta$, and d) $x = 16.9\delta$.

domain. This is not, however, the case for the locations in the inner part of the boundary layer. Overall, we may say that in the interaction region, and downstream of it, the excursions from the equilibrium value of $-R_{uT}$ are most pronounced close to the wall and become weaker with increasing distance from the wall. This corroborates the observation made in the discussion of Fig. 15 that throughout the interaction, the SRA relations hold reasonably well in the outer part of the boundary layer ($z > 0.5\delta$). For comparison, Fig. 16b plots $-R_{uT}$ at different wall-normal locations for the compression-ramp DNS of Wu and Martín [2]. The excursions from the equilibrium value are generally weaker than for the reflected-shock DNS. Also, no distinct minimum in the separation bubble is observed for $z = 0.5\delta$, 0.7δ, and 0.9δ, which may be attributed to the fact that the compression-ramp flow involves only a single shock wave, whereas the reflected STBLI configuration involves both the reflected shock and the incident shock.

B. Shock Motion

To analyze the shock motion further, we plot the intermittency of the wall pressure in Fig. 17. The intermittency is equal to the fraction of time that the shock spends upstream of a given streamwise location. Possible values thus lie between 0 and 1, where 0 means that the shock is at no time upstream of the particular streamwise location, and a value of 1 means that the shock is at all time upstream of the location. The intermittency in Fig. 17 is calculated using the following criterion. If the instantaneous wall pressure exceeds the upstream mean value by a significant amount (that is, if it lies above a certain threshold value), then the shock is considered to be upstream of that particular location; otherwise, it is considered to be downstream. In the present analysis, we use a threshold value of $1.13p_\infty$, which corresponds to $p_\infty + 4p_{\text{rms}}$, where p_{rms} refers to the value in the incoming boundary layer. An estimate for the streamwise extent of the shock motion may be obtained from Fig. 17 in one of several ways. The extent of the shock motion may be identified with the streamwise distance over which the value of the intermittency increases from, say, 0.1 to 0.9. Using this method, an estimate of 1.15δ is obtained. Alternatively, the extent of the shock motion may be identified with the inverse of the maximum slope of the intermittency plot. This gives a value of 1.14δ, which is similar to that found using the first method.

Figure 18a plots three different pressure signals for the DNS, all of which have been obtained at the same wall-normal coordinate $z = 1.6\delta$ but at different streamwise coordinates. The signals are spanwise-averaged, and the time duration shown corresponds to the full DNS data set. Except for turbulent fluctuations, the pressure signal at the most upstream of the three locations ($x = 6.7\delta$) displays no notable excursions from the freestream pressure $p/p_\infty = 1.0$. This indicates that the reflected shock does not cross this point at any time during the DNS; this point is located in the undisturbed incoming freestream. This must be contrasted with the point at $x = 10.0\delta$, which is located downstream of the reflected shock for the entire DNS. This is apparent from the fact that the mean pressure at $x = 10.0\delta$ is higher by a factor of approximately 2.4 than at $x = 6.7\delta$, which is consistent with the flow having passed through the shock. In addition, the turbulent fluctuations are stronger, owing to the turbulence amplification through the shock. Of most interest, however, is the pressure signal at $x = 9.1\delta$, located between the two positions already discussed. The signal is seen to vary intermittently between the upstream and downstream pressure levels, illustrating the motion of the reflected shock across this point.

The premultiplied power spectra for the pressure signals are shown in Fig. 18b. The spectra are normalized by the square of the local mean pressure, and they have been bin-smoothed using 100 bins. In the upstream undisturbed flow ($x = 6.7\delta$), most of the energy is contained in the frequency range of 0.1–$0.3U_\infty/\delta$ (~10–33 kHz), which is associated with the turbulent fluctuations (the upper bound of 33 kHz is, in fact, the Nyquist cutoff frequency, and the energetic range may well extend to higher frequencies). Inside the shock motion region ($x = 9.1\delta$), however, the most energetic frequencies are in the range of 0.002–$0.02U_\infty/\delta$ (~0.2–2 kHz), which is about 1 order of magnitude lower than the characteristic frequency of the turbulence in the incoming boundary layer. In the separated-flow region ($x = 10.0\delta$), the spectrum is quite flat, with significant energy at the low frequencies associated with the shock motion as well as at the high frequencies associated with the turbulence. Also note that

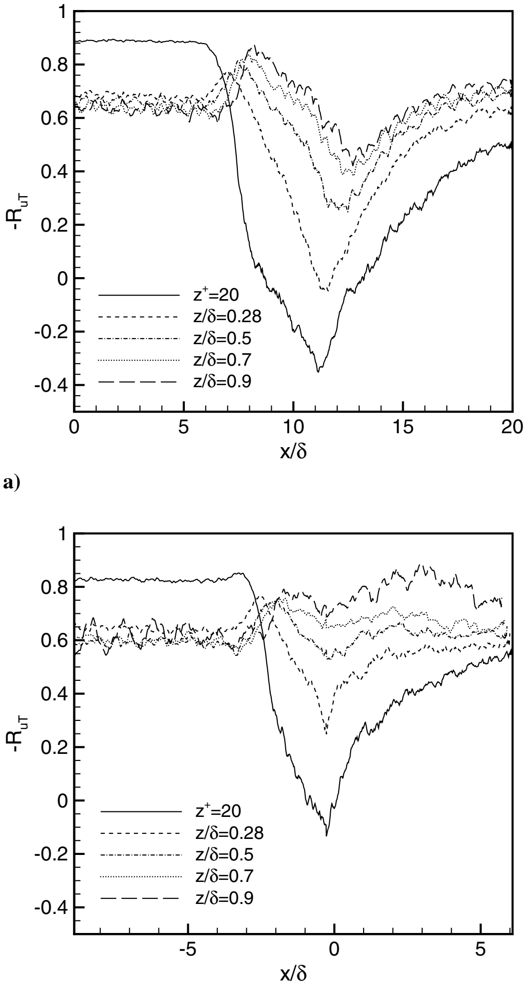

a)

b)

Fig. 16 SRA [Eq. (11)] at different wall-normal locations for a) the present DNS and b) the compression-ramp DNS of Wu and Martín [2].

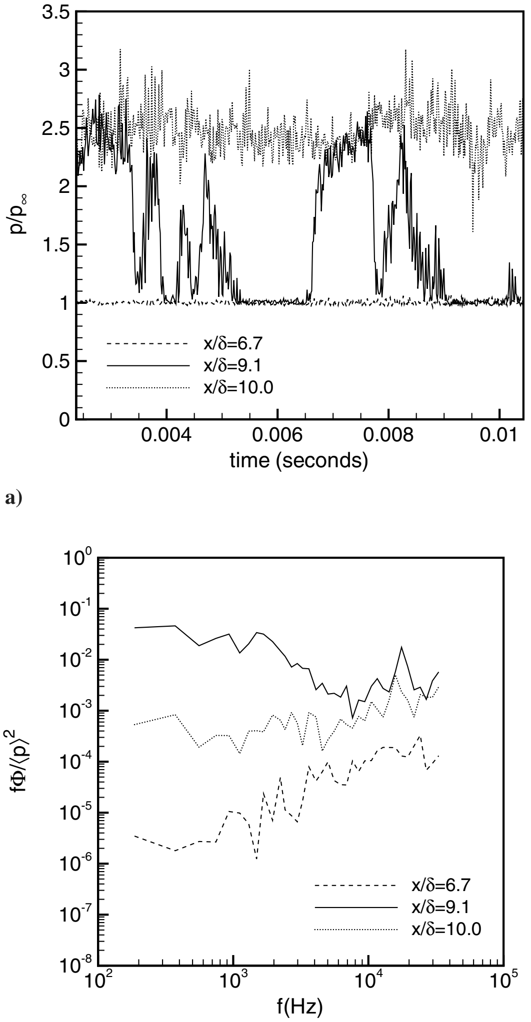

a)

b)

Fig. 18 Freestream pressure signals and corresponding spectra for different streamwise locations at $z = 1.6\delta$ for the DNS.

the spectrum for $x = 9.1\delta$ contains a significant, albeit not dominant, peak at the recycling frequency $0.22U_\infty/\delta$ (∼20.5 kHz). This forcing frequency lies in the range of frequencies associated with the turbulence in the incoming boundary layer, and it is 1–2 decades above the characteristic frequency of the shock motion.

The frequency of the shock motion is thus found to be 0.002–$0.02U_\infty/\delta$ from Fig. 18b, and this range agrees relatively well with that found from the wall-pressure spectra in Fig. 11b: namely, 0.002–$0.006U_\infty/\delta$. We should note, however, that the wall-pressure spectra have been computed with a total of 280,000 samples, in contrast to all the other statistics in this work, for which a much smaller number of samples (561) has been used. Consequently, the statistics in the low-frequency range of the wall-pressure spectra in Fig. 11b are converged, whereas those in Fig. 18b are not. Accordingly, more importance should be given to the results deduced from the wall-pressure spectra, and more statistics are required to draw conclusions from Fig. 18b.

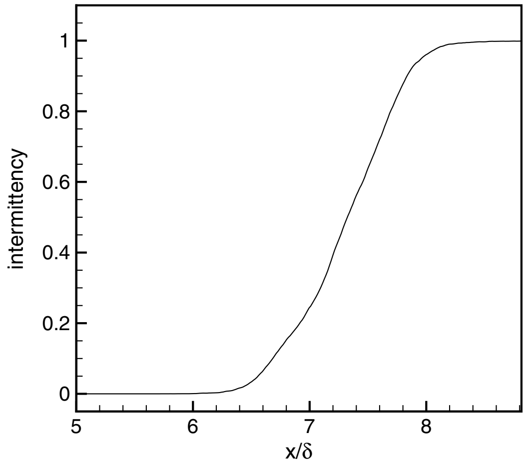

Fig. 17 Intermittency function computed from wall pressure for the DNS.

Figure 19 shows the same quantities as Fig. 18, except that the pressure signals are obtained further away from the wall at $z = 4.5\delta$. The three streamwise coordinates are changed accordingly to ensure that one point (namely, $x = 13.0\delta$) is located upstream of the reflected shock, another ($x = 15.1\delta$) is located inside the intermittent-shock-motion region, and the last one ($x = 17.0\delta$) is located downstream of the reflected shock. Because most of the preceding comments about Fig. 18 apply equally to Fig. 19, we merely point out a few notable differences. First, we note that the mean pressure at the most upstream location $x = 13.0\delta$ is $p/p_\infty = 2.3$ (and not $p/p_\infty = 1.0$). This is due to the fact that the flow has already passed through the incident shock. (See Fig. 4, in which at a wall-normal distance of $z = 1.6\delta$, the reflected shock is upstream of the incident shock due to the upstream influence, whereas it is the other way around at $z = 4.5\delta$, as the reflected shock is downstream of the incident shock.) Also note that given the proximity to the outlet of the computational domain, it is difficult to obtain a clean pressure signal that is fully downstream of the reflected shock. Consequently, the signal at $x = 17.0\delta$ still shows some intermittency.

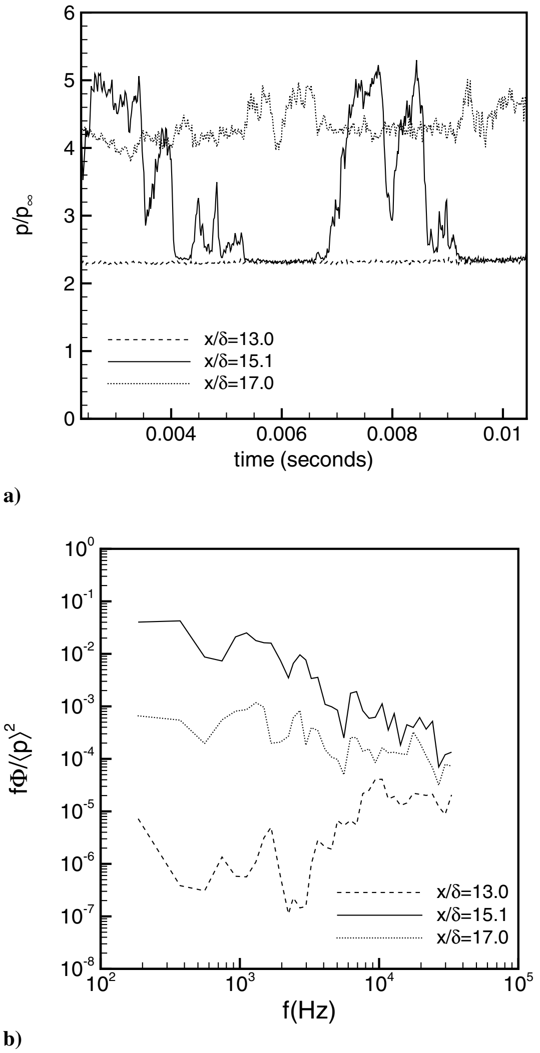

Fig. 19 Freestream pressure signals and corresponding spectra for different streamwise locations at $z = 4.5\delta$ for the DNS.

Comparison of the spectrum at $z = 1.6\delta$ and $x = 9.1\delta$ (shown in Fig. 18b) with the spectrum at $z = 4.5\delta$ and $x = 15.1\delta$ (shown in Fig. 19b) reveals an interesting aspect of the shock motion. Both spectra are obtained in the intermittent-shock-motion region, one near the foot of the shock close to the boundary-layer edge and the other further away from the wall in the freestream. The dominant low-frequency part of the spectra looks very similar, indicating that the low-frequency component of the shock motion is essentially unchanged as we move away from the wall. However, there are some differences in the high-frequency region associated with turbulence. Even if we neglect the peak at the recycling frequency, it is evident that at high frequency, the spectrum in the shock-foot region at $z = 1.6\delta$ and $x = 9.1\delta$ is more energetic than further away from the wall at $z = 4.5\delta$ and $x = 15.1\delta$. This observation is consistent with the earlier description of the shock motion as observed in a movie of subsequent instantaneous schlieren visualizations. The shock foot was seen to exhibit a high-frequency motion, and with increasing distance away from the wall, these high-frequency perturbations were seen to die out.

Figure 20 plots the intermittency of the pressure signals at $z = 1.6\delta$ and 4.5δ. Identifying the extent of the shock motion with the streamwise distance over which the value of the intermittency increases from 0.1 to 0.9, we estimate a value of 1.1δ at $z = 1.6\delta$ and 1.24δ at $z = 4.5\delta$. These estimates are similar to those obtained from the wall-pressure intermittency in Fig. 17. The relative lack of smoothness of the intermittency curves in the freestream (Fig. 20) as compared with that at the wall (Fig. 17) is due to the interpolation of the pressure field from the curvilinear computational grid onto planes $z = \text{const}$ and the small statistical sample size.

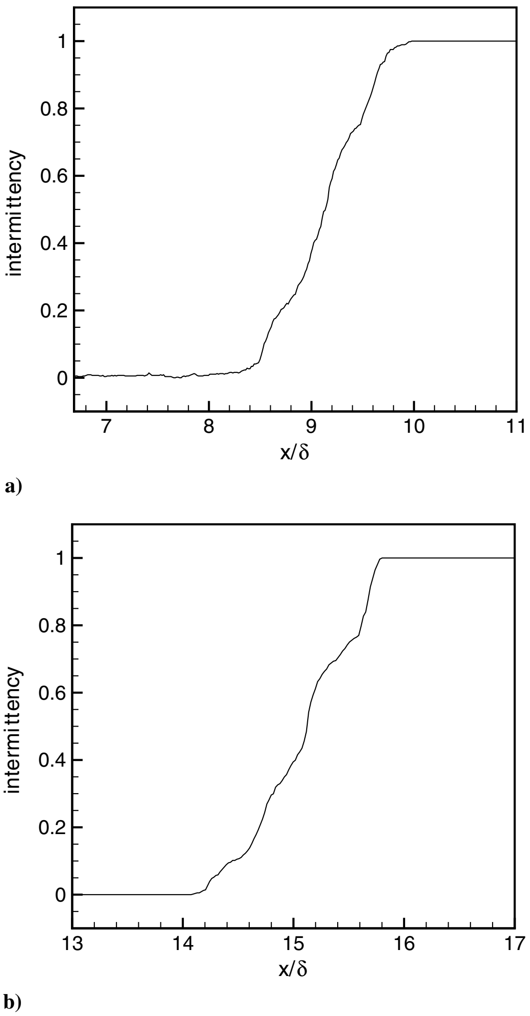

Fig. 20 Intermittency function computed from pressure signals at a) $z = 1.6\delta$ and at b) $z = 4.5\delta$ for the DNS.

Another method for analyzing the shock motion is by using a pressure-threshold criterion to detect the instantaneous shock location and then trace its evolution in time. For a given flowfield sample and at fixed y and z coordinates, we perform a sweep through the computational domain in the streamwise direction. The sweep starts at the inlet and stops as soon as the first point for which $p > p_{\text{threshold}}$ is encountered. That point is identified with the instantaneous shock location. The procedure is repeated for every spanwise location and for each of the 561 flowfield samples obtained from the DNS. Figure 21a plots the time trace of the reflected-shock location at two wall-normal locations: namely, $z = 1.6\delta$ and 4.5δ. Spanwise-averaging has been performed and the value of the shock location has been normalized by the local mean. At $z = 1.6\delta$, the value of the threshold is $p_{\text{threshold}}/p_\infty = 1.13$, and at $z = 4.5\delta$, it is 2.72, where the higher value is required because the flow at $z = 4.5\delta$ has already passed through the incident shock, whereas at $z = 1.6\delta$, it has not.

Figure 21a shows that the time traces of the shock location at the two wall-normal positions are very similar, displaying a predominantly low-frequency oscillation of the shock with amplitude of order δ. The only notable difference is that the signal has a richer high-frequency content in the shock-foot region at $z = 1.6\delta$ than further away from the wall at $z = 4.5\delta$. The spectra in Fig. 21b confirm that the signal at $z = 1.6\delta$ has a larger energy content in the high-frequency region. As previously noted, this is consistent with the high-frequency motions of the shock foot seen in schlieren animations of the DNS data. The dominant frequency, however, is once more found to be in the range of $0.002\text{–}0.01 U_\infty/\delta$ ($\sim$0.2–1.0 kHz) or about one order below the characteristic frequency of turbulent motions in the incoming boundary layer.

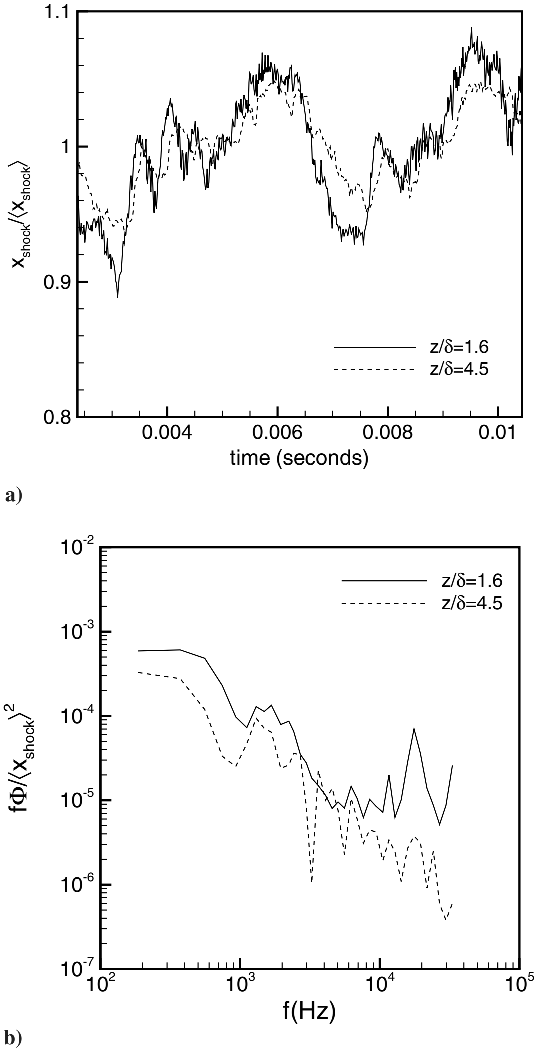

Fig. 21 Plots of a) location of the reflected shock as determined from a pressure-threshold criterion and b) corresponding spectra.

V. Conclusions

A DNS of a 12 deg reflected STBLI at Mach 2.9 and $Re_\theta = 2300$ is performed. For the spatial discretization of the inviscid fluxes, a linearly and nonlinearly optimized WENO scheme is used. Experimental results for the same configuration as in the DNS and at matching incoming flow conditions are available [7,8]. However, the flow in the experiments is seen to be highly-three-dimensional and, as a result, direct comparison with the DNS, which is homogeneous in the spanwise direction, is not possible. We stress, however, that because the DNS code is general and shock-location-independent and has been validated against experiments for the compression-corner case by Wu and Martín [2], we perform the present DNS with confidence.

The evolution of the mean and fluctuating quantities throughout the interaction is studied. The van Driest-transformed mean velocity profiles show a characteristic dip below the log law downstream of the interaction. At the exit of the computational domain, the dip is still present, indicating that the boundary layer does not fully recover to equilibrium within the extent of the computational domain. An important aspect of STBLI is the amplification of turbulence through the interaction. It is found that the mass-flux turbulence intensity is amplified by a maximum factor of 4 in the DNS; the Reynolds shear stress is amplified by a maximum factor of 21. We note that the mass-flux turbulence intensity is less amplified than in the compression-corner DNS of Wu and Martín [2]. Because the incoming flow conditions and overall shock strength are very similar in both simulations, we hypothesize that the difference in turbulence amplification is due to the significant streamline curvature in the compression-ramp DNS. The SRA is found to hold in the incoming boundary layer, whereas in the interaction region and downstream of it, there are significant departures from the SRA, particularly for $z < 0.5\delta$.

A movie of subsequent schlieren visualizations for the DNS reveals that the flow is strongly unsteady. The reflected-shock foot is seen to flap at a high frequency. Further away from the wall, in the freestream, the flapping has subsided, and the shock exhibits a large-scale low-frequency motion in the streamwise direction. The frequency of the shock motion is inferred to be 0.002–$0.006U_\infty/\delta$ from spectra of the wall pressure as well as from spectra of the pressure in the freestream. In nondimensional terms, this frequency corresponds to $S_L = f_s L_{\mathrm{sep}}/U_\infty = 0.015$–$0.046$, which lies in the range found in a survey of STBLI by Dussauge et al. [5]. From the intermittency of the pressure signals, the streamwise extent of the shock motion is found to be of order δ. Touber and Sandham [11] performed LES of the reflected-shock case with varying spanwise domain sizes. They found that reducing the spanwise length to very narrow domains results in increased separation length due to the high level of spanwise coherence. In particular, reducing the domain width below 1.4δ significantly affects the separation length, and a reduction of 50% in the spanwise dimension (from 1.4δ) results in a 36% increase of the separation length. In contrast, they found that the separation length asymptotes when increasing the domain size beyond 1.4δ. In fact, increasing the spanwise direction to 5 times 1.4δ only reduces the separation length by 13%. Our spanwise domain size here is 2δ, and the size of the separation length agrees well with empirical scaling of Dussauge et al. [5].

The physical mechanism that drives the shock motion in the DNS remains to be studied.

Acknowledgment

This work is supported by the U.S. Air Force Office of Scientific Research under grant AF/9550-06-1-0323.

References

[1] Smits, A. J., and Dussauge, J. P., *Turbulent Shear Layers in Supersonic Flow*, 2nd ed., Springer Verlag, New York, 2006.

[2] Wu, M., and Martín, M. P., "Direct Numerical Simulation of Supersonic Turbulent Boundary Layer over a Compression Ramp," *AIAA Journal*, Vol. 45, No. 4, 2007, pp. 879–889. doi:10.2514/1.27021

[3] Wu, M., and Martín, M. P., "Analysis of Shock Motion in Shockwave and Turbulent Boundary Layer Interaction Using Direct Numerical Simulation Data," *Journal of Fluid Mechanics*, Vol. 594, 2008, pp. 71–83. doi:10.1017/S0022112007009044

[4] Green, J. E., "Reflexion of an Oblique Shock Wave by a Turbulent Boundary Layer," *Journal of Fluid Mechanics*, Vol. 40, 1970, pp. 81–95. doi:10.1017/S0022112070000058

[5] Dussauge, J. P., Dupont, P., and Debiève, J. F., "Unsteadiness in Shock Wave Boundary Layer Interactions with Separation," *Aerospace Science and Technology*, Vol. 10, No. 2, 2006, pp. 85–91. doi:10.1016/j.ast.2005.09.006

[6] Dupont, P., Piponniau, S., Sidorenko, A., and Debiève, J. F., *AIAA Journal*, Vol. 46, No. 6, 2008, pp. 1365–1370. doi:10.2514/1.30154

[7] Bookey, P. B., Wyckham, C., Smits, A. J., and Martín, M. P., "New Experimental Data of STBLI at DNS/LES Accessible Reynolds Numbers," AIAA Paper 2005-309, Jan. 2005.

[8] Bookey, P. B., Wyckham, C., and Smits, A. J., "Experimental Investigations of Mach 3 Shock-Wave Turbulent Boundary Layer Interactions," AIAA Paper 2005-4899, June 2005.

[9] Ringuette, M. J., Bookey, P., Wyckham, C., and Smits, A. J., "Experimental Study of a Mach 3 Compression Ramp Interaction at $Re_\theta = 2400$," *AIAA Journal*, Vol. 47, No. 2, 2009, pp. 373–385. doi:10.2514/1.38248

[10] Garnier, E., Sagaut, P., and Deville, M., "Large Eddy Simulation of Shock/Boundary-Layer Interaction," *AIAA Journal*, Vol. 40, No. 10, 2002, pp. 1935–1944. doi:10.2514/2.1552

[11] Touber, E., and Sandham, N. D., "Oblique Shock Impinging on a Turbulent Boundary Layer: Low-Frequency Mechanisms," AIAA Paper 2008-4170, June 2008.

[12] Pirozzoli, S., and Grasso, F., "Direct Numerical Simulation of Impinging Shock Wave/Turbulent Boundary Layer Interaction at $M = 2.25$," *Physics of Fluids*, Vol. 18, No. 065113, 2006.
doi:10.1063/1.2216989

[13] Ringuette, M. J., Wu, M., and Martín, M. P., "Low Reynolds Number Effects in a Mach 3 Shock Turbulent Boundary Layer Interaction," *AIAA Journal*, Vol. 46, No. 7, 2008, pp. 1883–1886.
doi:10.2514/1.36213

[14] Ringuette, M. J., and Smits, A. J., "Wall-Pressure Measurements in a Mach 3 Shock-Wave and Turbulent Boundary Layer Interaction at a DNS-Accessible Reynolds Number," AIAA Paper 2007-4113, June 2007.

[15] Martín, M. P., Taylor, E. M., Wu, M., and Weirs, V. G., "A Bandwidth-Optimized WENO Scheme for the Direct Numerical Simulation of Compressible Turbulence," *Journal of Computational Physics*, Vol. 220, No. 1, 2006, pp. 270–289.
doi:10.1016/j.jcp.2006.05.009

[16] Taylor, E. M., Wu, M., and Martín, M. P., "Optimization of Nonlinear Error for Weighted Essentially Non-Oscillatory Methods in Direct Numerical Simulations of Compressible Turbulence," *Journal of Computational Physics*, Vol. 223, No. 1, 2006, pp. 384–397.
doi:10.1016/j.jcp.2006.09.010

[17] Xu, S., and Martín, M. P., "Assessment of Inflow Boundary Conditions for Compressible Boundary Layers," *Physics of Fluids*, Vol. 16, No. 7, 2004, pp. 2623–2639.
doi:10.1063/1.1758218

[18] Martín, M. P., "Direct Numerical Simulation of Hypersonic Turbulent Boundary Layers. Part A: Initialization and Comparison with Experiments," *Journal of Fluid Mechanics*, Vol. 570, 2007, pp. 347–364.
doi:10.1017/S0022112006003107

[19] Délery, J., and Marvin, J. G., *Shock-Wave Boundary Layer Interactions*, AGARD AGARDograph No. 280, Neuilly-sur-Seine, France, 1986.

[20] Green, J. E., "Interaction Between Shock Waves and Turbulent Boundary Layers," *Progress in Aerospace Sciences*, Vol. 11,1970, pp. 235–260.
doi:10.1016/0376-0421(70)90018-7

[21] Smits, A. J., and Muck, K. C., "Experimental Study of Three Shock Wave/Turbulent Boundary Layer Interactions," *Journal of Fluid Mechanics*, Vol. 182, Sept. 1987, pp. 291–314.
doi:10.1017/S0022112087002349

S. Fu
Associate Editor